RWTH Aachen University

Joint Master Applied Geophysics [2021-2023]

2D synthetic geophysical multi-method imaging study of a simplified volcanic diatreme structure

Anton Ziegon: 21-958-970

Report submitted for Research Module (Module 54.12000)

Supervisors:

Supervisor 1: Prof. Dr. Florian Wagner RWTH Aachen University
Supervisor 2: Dr. Marc Boxberg RWTH Aachen University

January 22, 2023

Abstract

This paper presents a 2D synthetic imaging study of a simplified volcanic diatreme structure in a layered subsurface. It is designed to mimic a potential diatreme structure of a phonolitic eruption center as it is expected in the region of the Rockeskyller Kopf in the Westeifel, Germany. In the upcoming Master research project, acquired field data will be jointly inverted to model the volcanic eruption center in order to improve existing knowledge about the geologic history of the study area. Goal of this study is to investigate the sensitivity as well as its limitations of different geophysical methods to such a geologic structure. Therefore, it will help to understand the information content in the data sets which will be useful for the inversions as well as for additional data acquisition. The synthetic study includes electrical resistivity tomography (ERT), traveltime tomography and gravity data. Model construction, forward calculations and data inversion is performed using the open-source library pyGIMLi (Rücker et al., 2017). The material properties of the forward model are based on previously acquired data of the region around the Rockeskyller Kopf as well as typical values found in the literature. ERT and traveltime inversion results represent a error-weighted, smoothness-constrained least-squares solution to the inverse problem and are determined using the corresponding routine in pyGIMLi. The results show a good representation of the subsurface geometry. The best results are obtained by the Dipole-Dipole ERT configuration, however, the influence of noise suggests that complementary methods or electrode configurations need to be acquired in the field. Due to the irregular diatreme boundaries as well as an unfavorable low velocity of the diatreme, the method is lacking to image the inside of the structure homogeneously which makes an accurate interpretation more difficult. The modeled gravity response of the subsurface also suggests that additional gravity data can be acquired in the field to add more information about deeper parts of the structure as the ERT and traveltime tomography methods are limited to the shallow subsurface. This study also stresses the influence of regularization parameters during data inversion and the importance of a sophisticated choice of the parameters as it has a strong influence on the final images.

1 Introduction

The western part of the Eiffel region is known for strong volcanism in the past one million years (Schmincke, 2009). This work focuses on the region close to the Rockeskyller Kopf as it differs from the surrounding volcanism. First huge sanidine crystals were found in the 1920s (Hopmann, 1914) and studied since then. The mineralogical analysis indicates a phonolitic eruption close to a highly differentiated magma which is atypical for the study area (Boxberg, 2011).

A potential explanation could be that during a phonolitic eruption magmatic tuffs as well as fragments of the neighbouring host rock are emitted. Most of the erupted material is assumed to fall back into the crater and therefore highly fractured rocks and magmatic tuffs are found inside the diatreme structure (White et al., 2011). Due to surface erosion and deposition of new sediments the crater is buried under a new geologic layer and cannot necessarily be identified with geomorphologic analysis. Therefore, non-intrusive geophysical methods have to be applied in order to reveal those structures. Finding and modelling the volcanic eruption center of this phonolitic eruption will help to improve the existing knowledge about the regional geology of the Westeifel around the Rockeskyller Kopf.

The first efforts to find the volcanic source of these sanidine crystals are documented in Mertes (1983). The author conducted a magnetic survey which indicates a strong anomaly. Several follow-up geophysical surveys using magnetics, seismic methods and electrical resistivity tomography (ERT) were conducted in order to find and model the volcanic structure in the subsurface (Boxberg, 2011; Mues, 2013; Plumpe, 2015; Hauburg, 2016; Schneider, 2017; Gilberti, 2020). First initial models are mainly based on the magnetic measurements, however, a more detailed model of the volcanic source is yet to be determined.

Goal of the upcoming Master thesis is to obtain a more detailed subsurface model of the volcanic structure which is indicated by the strong magnetic anomaly described in Boxberg (2011) and Mertes (1983). Using joint inversion approaches a geologic model of the volcanic diatreme based on several geophysical methods will be generated. To better understand the sensitivity of the different methods to a diatreme structure in the subsurface, this report presents a synthetic study of a representative diatreme structure as it could be found in the field. For model generation, forward calculations and data inversion the open-source library pyGIMLi (Rücker et al., 2017) is used. The synthetic imaging study includes the ERT method, seismic refraction tomography and gravimetric data. The synthetic imaging study will show which parts of the subsurface structure can be retrieved from the different geophysical methods and how the different methods compare with each other.

The forward model used in this synthetic imaging study is designed to mimic a typical diatreme structure. To simplify the model generation and to speed up forward calculations and inversions, a 200 m long and 70 m deep 2D section through a simplified diatreme structure is considered. The forward model is based on White et al. (2011) as well as first subsurface models based on the geophysical surveys that were mentioned before. To consider a more realistic scenario the diatreme structure shows an irregular upper boundary and is hosted in a horizontally layered subsurface consisting of a shallow soil layer, two sandstone layers and the basement. The resulting 2D section is shown in 1 and it is used to produce synthetic data with the in section 2 described methods.

2 Methods

2.1 Mesh generation

To discretize the 2D subsurface geometry (Figure 1), especially the diatreme structure, as good as possible, an unstructured, triangular mesh is used. This is done in pyGIMLi by using the function

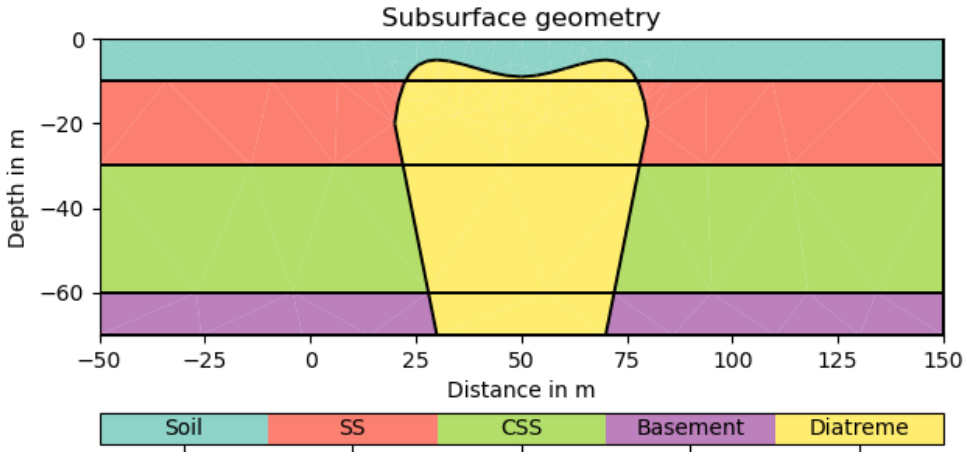

Figure 1: Synthetic model of simplified diatreme structure. SS is referring to the first sandstone layer and CSS refers to a second, more consolidated sandstone layer.

Table 1: Material properties of different geologic formations.

Formation	**P-wave Velocity** $[m/s]$	**Electrical Resistivity** $[\Omega m]$	**Density** $[kg/m^3]$
Soil	650	120	1250
SS	3000	1200	2400
CSS	3600	3500	2500
Basement	4500	10^8	2650
Diatreme	2000	10^5	2100

pygimli.meshtools.createMesh() which is calling the two-dimensional quality mesh generator and Delaunay triangulator *Triangle* (Shewchuk, 1996). The resulting mesh is shown in Figure 2 and consists mainly of triangles with a ratio of shortest to longest edge close to 1 and is therefore suitable for finite element calculations. The big benefit of the unstructured mesh is that it can discretize curved or irregular boundaries better than a rectangular grid and therefore ensures a better accuracy when running calculations on the model. As a discretization of the diatreme structure with a rectangular grid would result in steps at the boundaries, rectangular grids were not considered.

Different material properties, i.e. seismic P-wave velocity, electrical resistivity and density, are assigned to the different geologic formations that are indicated in Figure 1. The values are based on previous geophysical studies of the area as for example Gilberti (2020) and Plumpe (2015) and further literature like Geldart et al. (2004) and Palacky (1988) and summarized in table 1. The upper sandstone layer (SS) is assumed to be part of the groundwater aquifer and therefore has a much lower resistivity than the more consolidated and dense sandstone layer below (CSS). As it is to be expected, the basement can be characterized as a high-velocity, high-resistivity and high-density formation, while the soil layer represents the opposite trend. As highly fractured rock is assumed to be inside the diatreme structure, a comparably low velocity and density was chosen and a smaller resistivity value than it is usual for andesitic magmatic rocks. This model will be used as an input for the gravimetric, ERT and SRT forward calculations which are presented in the following sections.

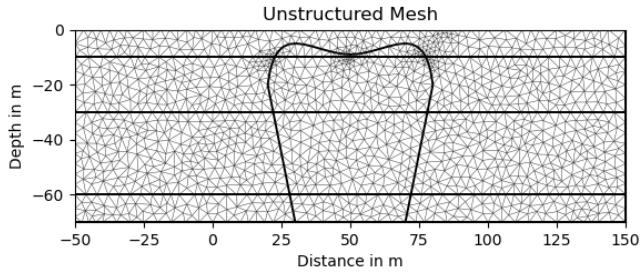

Figure 2: Unstructured, triangular mesh used to discretize the subsurface geometry.

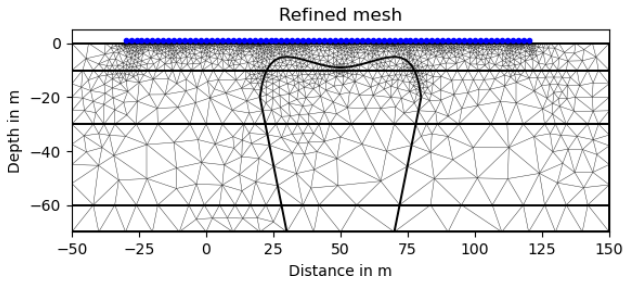

Figure 3: Refined mesh used for ERT calculations. Electrode locations are presented in blue.

2.2 Electrical Resistivity Tomography

The ERT method is sensitive to electrical resistivity contrasts in the subsurface which arise from, for example, changes in clay content, porosity, pore fluid or ore minerals. A direct current is inserted into the ground using two electrodes and the potential difference between two points is measured with two additional electrodes. The observed potential difference can be used to retrieve an image of the subsurface resistivity distribution via inverse methods. The electric potential U is defined by the Poisson equation:

$$\nabla[\sigma(\mathbf{r})\nabla U(\mathbf{r})] = -\nabla J. \tag{1}$$

Here, $\mathbf{r}$ stands for the location, J for the injected electrical current, and σ for the electrical conductivity which is the inverse of the electrical resistivity ρ. This equation builds the basis for the ERT forward calculation (Johnson et al., 2015). For a known conductivity distribution, a known injected current and appropriate boundary conditions at the model boundaries, the potential at every location inside the model can be calculated.

The calculation is performed using the module *pygimli.physics.ert* (Günther et al., 2006; Rücker et al., 2006). It assumes a Neumann boundary condition (i.e. a fixed derivation of the potential) for the upper boundary as its is representing the free surface boundary of the Earth. For the remaining boundaries, a mixed boundary condition is implemented to avoid unpyhsical field distortions and ensure accuracy of the simulation. Using information defined in *ert.scheme*, a finite element simulation can be run to determine the electrical potential in the modelling domain. To ensure numerical accuracy close to the current injection locations as well as the potential measurement locations, a refinement of the mesh is performed. The refined mesh is shown in Figure 3. Note that the new mesh has smaller cells close to the surface where the virtual electrodes are located and bigger cells in greater depth. That is done to ensure higher accuracy close to injection points which is crucial for the simulation of the whole model domain.

Using the results of the simulations, the potential differences between two virtual electrodes for two virtual injecting electrodes can be calculated. This can be converted to apparent resistivity ρ_{app} according to Kearey et al. (2002) as follows:

$$\rho_{app} = \frac{2\pi}{\frac{1}{\overline{AM}} - \frac{1}{\overline{AN}} - \frac{1}{\overline{BM}} + \frac{1}{\overline{BN}}} \frac{\Delta U}{I} = K\frac{\Delta U}{I} \tag{2}$$

ΔU represents the potential difference between the two measurement locations M and N, I stands for the strength of the injected electrical current between the locations A and B. The distance between an injection point and a measurement point is represented for example by $\overline{AM}$. The factor related to the acquisition geometry is also often referred to as the geometrical factor K. To create a more realistic

data set, noise is added to the data inside the *simulate()* function. The noise is random and is defined by an absolute value as well as a noise level. The noise level is given in percent and defines the relative noise magnitude on a data point. The absolute noise on the other hand defines a noise magnitude independent from the data point and is therefore defined in volt (V). For each data point, the largest of those noise criteria is chosen to define the noise which will the contaminate the data.

After generating the synthetic data as described above an inversion is performed in order to turn the apparent resistivity section into a true resistivity distribution. This is done via the function *pygimli.frameworks.methodManager.invert()*. This function requires the generated synthetic data as input as well as parameters for the inversion mesh generation and the inversion. The function is starting the inversion process by constructing an inversion mesh based on the acquisition geometry and the additional parameters given as an input. The inverse problem is subject to a non-linear optimization problem as the misfit function χ needs to be minimized. The misfit criterion χ is calculated using the synthetic data and the predicted data. A value of approximately $\chi = 1$ is desirable as it represents a model that explains the data within the uncertainties or error estimates. Using a Gauss-Newton algorithm an error-weighted, smoothness-constrained least-squares solution to the inverse problem is determined which can be visualized as a resistivity distribution. The smoothness constraint is mainly controlled through the regularization parameter λ, which weights between the data fit χ and the model smoothness. The higher the λ value, the smoother is the resulting model. However, it results in a worse data fit (Rücker et al., 2017).

2.3 Seismic Refraction Tomography

Seismic refraction tomography (SRT) is a method that is based on seismic refraction in the subsurface. Refracted waves occur if a seismic velocity increase can be observed with increasing depth. In that case the wave is travelling faster inside the deeper refractor in comparison with the direct wave which is travelling along the surface such that, at a certain distance, the refracted wave is overtaking the direct wave. Then the first arrival in the seismic measurements is contributed by the refracted wave (Kearey et al., 2002). Synthetic SRT data is created using the standard routine in the module *pygimli.physics.traveltime*, starting with the setup of the acquisition geometry. Then, a refined mesh is constructed similar to the ERT calculations described in section 2.2. The synthetic data is generated via the function *pygimli.physics.traveltime.TravelTimeManager.simulate()* which will first computes the ray paths between sources and sensors. With known ray paths the synthetic data in form of traveltimes can be calculated according to Zelt (2021) as:

$$t_i = \sum_j l_{ij} sj. \tag{3}$$

t_i is the i-th taveltime observation, l_{ij} the length of the i-th ray path segment (corresponding to the i-th observation) in the j-th model cell and s_j is the slowness of the j-th model cell. Note that the slowness s is the reciprocal of the velocity v. Noise is defined similar as it was already described for the synthetic ERT data. Important to mention is that the absolute noise is defined in seconds (s) as traveltimes are generated.

After generating the synthetic traveltimes, an inversion of the data is performed similar to the ERT data inversion described in section 2.2. An inversion of the traveltime data is performed by calling the function *pygimli.physics.traveltime.TravelTimeManager.invert()*. Like the ERT inversion,the result is an error-weighted, smoothness-constrained least-squares solution in form of a velocity model that explains the data within the uncertainties (Rücker et al., 2017).

2.4 Gravimetry

The gravity method is based on Newton's Law of Gravitation which relates the force F between two bodies with their masses m_1 and m_2 and the distance r between them as:

$$F = \frac{Gm_1m_2}{r^2}. \tag{4}$$

The constant G is called the gravitational constant and holds a value of $6.67 \cdot 10^{-11} m^3 kg^{-1} s^{-2}$. Assuming that one body is the Earth with a mass M and a radius R, the gravitational force on an object on the Earth surface would be:

$$F = \frac{GM}{R^2} m = gm. \tag{5}$$

As shown in the equation 5 the gravitational force on a body is a product of the gravitational acceleration g, often also referred to as gravity, and its mass. In gravimetry it is most useful to describe the gravitational field in form of its potential U as the gravitational acceleration is the negative gradient of the potential U. The magnitude of the potential depends on the radius as well as on the density distribution in the subsurface and therefore measurements of the gravitational acceleration can be used to gain knowledge of subsurface structures (Kearey et al., 2002).

A synthetic gravity study of the simplified diatreme model is performed by applying the function *pygimli.physics.gravimetry.solveGravimetry()* to the mesh with a defined sensor geometry and density distribution. The forward calculation of the gravimetric potential is performed after Won et al. (1987). The synthetic data shows then the gravitational response of the density distribution. To isolate the gravity response of the anomaly synthetic data of the layered subsurface without the diatreme structure will be generated and deducted from the first simulation data. The resulting data shows the effect of the diatreme structure on the gravitational acceleration which equals the first derivative of the gravitational potential. As pyGIMLi does not offer a fast and easy way yet to invert gravity data in 2D and due to the lack of time during the research module, the synthetic gravity data is not inverted in this work. However, the synthetic data will be visualized and discussed in the sections 3 and 4.

3 Results

A summary of all settings used for the forward and inverse calculations is presented in the appendix in tables A1 and A2. In the following subsections a reasoning for these parameters will be presented and results will be shown.

3.1 Electrical Resistivity Tomography

For the ERT data generation, 76 synthetic electrodes over a distance of 140 m are used to simulate the potential differences. These values are chosen as they represent a realistic field setup as it could be done as part of a thesis work. The same reasoning is also used for the other methods. Three different electrode configurations are simulated, namely the Dipole-Dipole, Schlumberger and Wenner configuration. The noise level is defined with 2.5% and the absolute value of 0.001 mV. As the absolute noise is set very low, the data is contaminated by the relative noise magnitude. The resulting data can be visualized in terms of apparent resistivity in a pseudo section. This is shown in Figure 4 in the top row. Since no topography is considered the pseudo section directly indicates a strong subsurface anomaly as the apparent resistivities are varying between 100 Ωm and 1000 Ωm. We can also see that the Dipole-Dipole configuration is generating the most data points as it shows the most cells in the section.

Using the respective parameters in table A2, an inversion of the data is performed. The settings for the inversion are found by trial and assumed to be good as the data misfit value χ^2 is close to 1 for all three configurations. The estimated ERT data in shown in the bottom row of Figure 4 and no significant difference between the observed and estimated pseudo sections can be observed. The resulting inverted resistivity sections are presented in Figure 5. It can be seen that all three configurations do not hold significant information below a depth of 40 m. They show a strong high-resistivity anomaly in the centre of the section at a depth between approximately 10 m and 30 m that is reaching resistivities over 10000 Ωm. A shallow very conductive layer is shown up to a depth of around 10 m. Left and right of the strong resistive anomaly and below the conductive top layer another unit with resistivities of around 1000-2700 Ωm can be identified. Important to mention is that the Dipole-Dipole result appears to show slightly higher resistivity values below the conductive top layer but this is produced by the plotting. The Dipole-Dipole configuration has more measurements resulting in a higher coverage and therefore less transparent model cells. A more detailed discussion of the final inversion results of the different ERT configurations is presented in section 4.

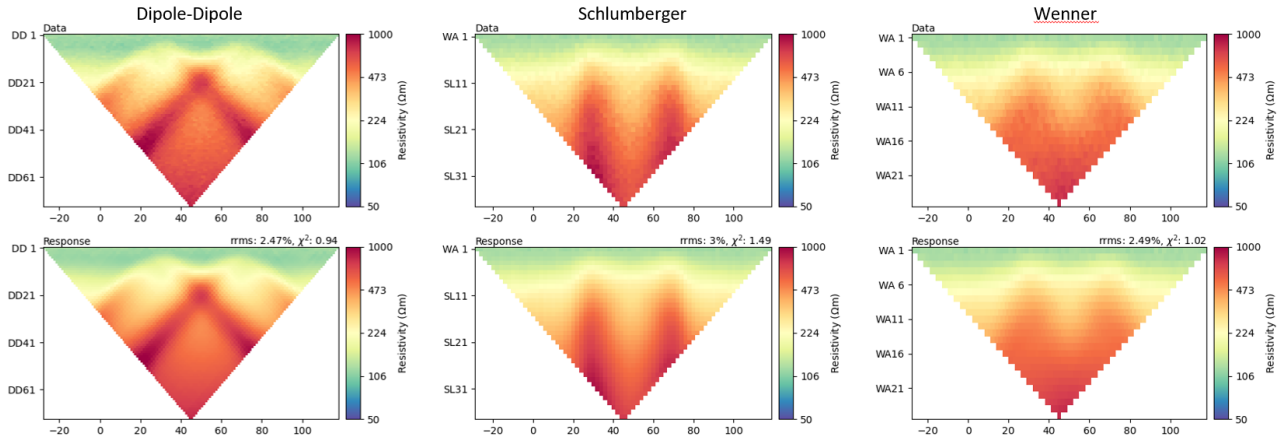

Figure 4: Inversion result misfit of the Dipole-Dipole (left), Schlumberger (middle) and Wenner electrode configuration. At the top the synthetic data pseudo section is shown and below the pseudo section resulting from the inversion is presented. On top of the inverse model response the root mean square error (RMS) and the data misfit χ is stated.

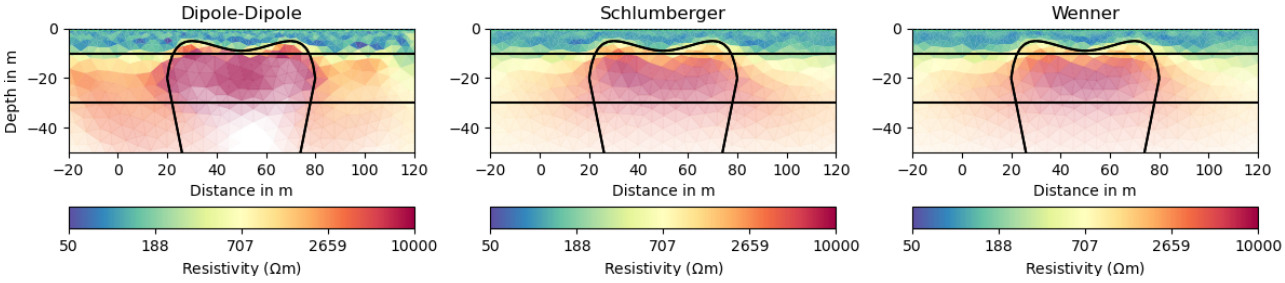

Figure 5: Final ERT inversion results. The results of the Dipole-Dipole (left), Schlumberger (middle) and Wenner configuration (right) are superimposed by the subsurface geometry used for synthetic data generation. The transparency of the mesh cells indicates the data coverage as opaque cells represent higher data coverage.

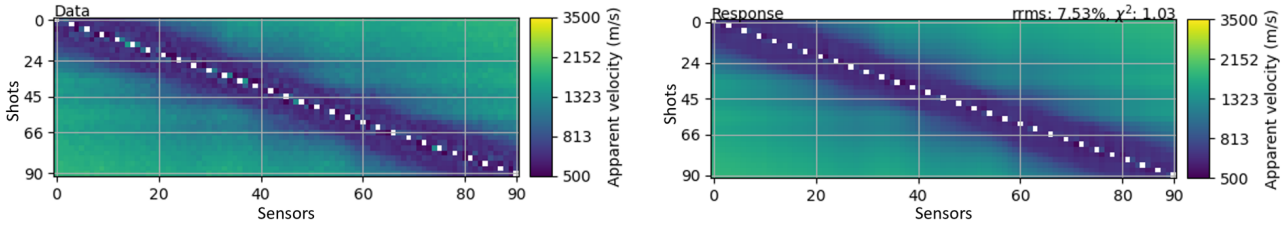

Figure 6: Inversion result misfit of the synthetic seismic refraction tomography data. On the left, the synthetic data is shown and, on the right, the estimated data resulting from the inversion is presented. On top of the inverse model response, the root mean square error (RMS) and the data misfit χ is stated.

3.2 Seismic Refraction Tomography

For the traveltime data generation 91 sensors with a spacing of 2 m are defined between -40 m and 140 m. Every third sensor location is chosen to be a shot location, resulting in 31 shots. Just as the synthetic ERT data, noise is produced and added to the generated data. For the SRT data the absolute noise is set to 1 ms and the relative noise to 0.01 %. This means that for early arrivals (i.e. small source-receiver offsets) the absolute noise is defining the noise magnitude while for later arrivals (i.e. large offsets) the relative noise parameter is the deciding factor. The synthetic data is presented in the left part of Figure 6. In the data matrix, the zero offset measurements (i.e. measurements with an identical source and receiver location) are excluded and appear white. The simulated traveltimes are directly converted to apparent velocities using the source receiver distance.

The inversion of the synthetic traveltimes results in an estimated data matrix which is shown in the right part of Figure 6. As seen, the data misfit is very close to one and therefore an acceptable inversion result can be assumed. Figure 7 presents the resulting velocity model on the left and the corresponding ray coverage on the right. As seen in the right plot, the data does not hold any information about the subsurface below 30 m depth as well as close to the left and right model boundary. Therefore, the model values in these regions are not reliable as they are not data driven but purely depending on the initial model of the iterative inversion scheme. Note that this part of the model space will not be discussed further as it does not contribute to the objectives of this synthetic data study. In the upper 10 m of the model we find a low-velocity layer which holds velocities below 1000 m/s. Between -20 m and 20 m as well as between 80 m and 120 m at a depth of 10 m to 30 m, high-velocity structures appear with velocities of 3000-3500 m/s. In between those high-velocity anomalies two velocity anomalies with around 1500 m/s (at a distance of 20-40 m and 60-80 m) appear. Between 40 m and 60 m a structure with approximately 2900 m/s can be observed. Further discussion of the results and a comparison with the other methods is presented in section 4.

3.3 Gravimetry

According to table A1 the synthetic gravity data was generated using a 140 m long spread of 71 stations. As no inversion is performed on this synthetic data set, no noise is generated and superimposed on the data. The synthetic gravity measurements can be seen in Figure 8. As the parameter table 1 states, the diatreme has a lower density than the surrounding dense sandstone and therefore produces a negative gravity response in the synthetic data. Due to the irregular upper boundary of the diatreme structure two saddle points in the gravity anomaly can be observed at 30 m and 70 m. Figure 8 also shows that the anomaly reaches its maximum magnitude of approximately -0.3 mGal at a distance of 50 m which coincides with the center axis of the diatreme structure.

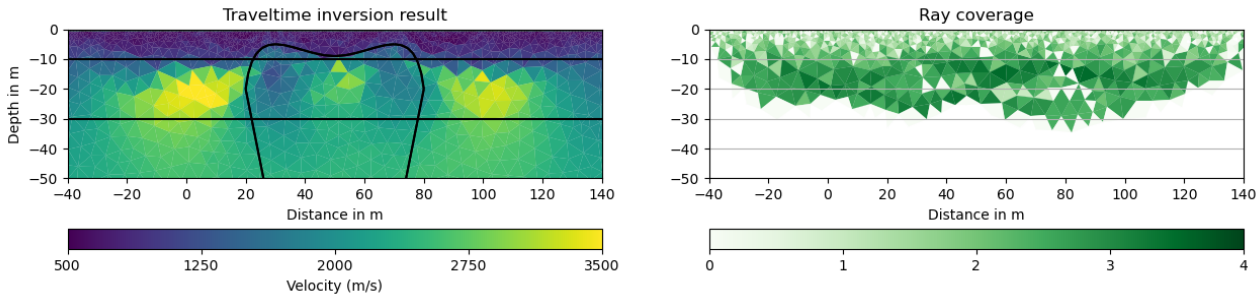

Figure 7: Final traveltime inversion results. The final velocity model (left) is superimposed by the subsurface geometry used for synthetic data generation. The ray coverage of the SRT is shown on the right.

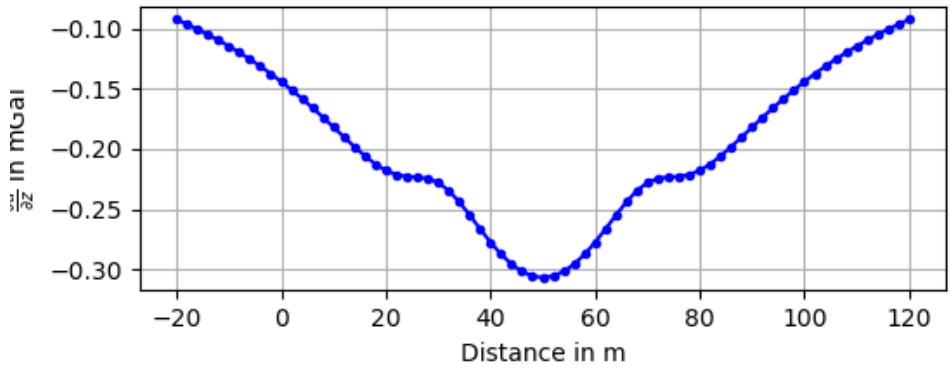

Figure 8: Synthetic gravity data points.

4 Discussion

As seen in Figure 5 all three configurations result in a similar subsurface resistivity distribution. Comparing them to the superimposed initial starting model that was used for the data generation, all ERT inversions results represent the upper soil layer as well as the upper part of the diatreme structure accurately. However, there a differences observable between the Dipole-Dipole and the remaining two configuration as the Soil layer appears to be more homogeneous for the Schlumberger and Wenner configuration when comparing it to the Dipole-Dipole result. This is resulting from the noise and the inversion settings. As the Dipole-Dipole configuration has more measurements overall more data is involved in the inversion process. In order to reach a data misfit of approximately $\chi^2 = 1$, the smoothing parameter λ was comparably low with a value of 3 which implies less smoothing and a higher variance of the model parameter. This on the other hand allows the model parameters to appear in a more geologic way as a less smooth transition between soil, sandstone and diatreme can be observed. This is desirable as the boundaries of the diatreme, especially the ones on the sides, are retrieved slightly better when comparing it to the other two configurations. In this case, the inversion parameters are found by trial and error to reach a data misfit close to 1. A more sophisticated approach for determining the value of the regularization parameter, like the L-curve criterion, is not used in this project due to the limited amount of time, however, it could improve inversion results of the Schlumberger and Wenner configuration towards a slightly better fit with the initial starting model (Lawson et al., 1995).

The soil layer can be retrieved quite accurately from the synthetic traveltime data which can be derived

from Figure 7. Using the superimposed synthetic subsurface geometry, the high-velocity structures that are mentioned in section 3.2 can be identified as the upper sandstone layer. Due to no ray coverage at the model boundaries the high-velocity structures appear more like an elliptic object rather than a horizontal layer. The upper boundary as well as the left boundary of the diatreme structure are imaged properly, while the right side of the diatreme shows a more gradual transition which makes the interpretation of the boundary position more difficult. As already discussed for the ERT inversion result, this smooth transition could be improved by investigations of the regularization parameter λ. The traveltime inversion images the insides of the diatreme rather heterogeneous in form of two medium and one high-velocity region. Averaging the inside of the diatreme structure returns a good approximation of the true velocity, however, without the superimposed subsurface geometry an interpretation would probably result in several structures rather than combining all three anomalies in one structure. A possible reason for the lack of imaging of the inside of the diatreme is the comparably low velocity. During traveltime tomography, rays are circumventing low-velocity regions which results in a lower data coverage and less reliable values. As the diatreme has a lower velocity than the surrounding sandstone, the sides of the diatreme are sensed less by the virtual rays and therefore could cause the lack of imaging. This reasoning is supported by the ray coverage plot on the right of Figure 7 as the low-velocity regions coincide with lower ray coverage. Especially close to the right boundary of the diatreme at a distance of approximately 80 m, several cells without ray coverage can be observed.

After discussing the results of the ERT and traveltime inversion separately the methods are now compared with each other. Both methods are able to accurately recover the upper soil layer as well as the upper boundary of the diatreme. They also return accurate estimates for the resistivity and velocity of the soil and sandstone layer. The ERT method resolves the lateral boundaries of the diatreme structure slightly better and images the diatreme as a homogeneous structure which the traveltime tomography is lacking. Especially the Dipole-Dipole configuration images the diatreme boundaries accurately but is prone noise in the measurements. The traveltime tomography as well as the other two ERT configurations are more robust but perform slightly worse in the imaging of the diatreme. In the field, the traveltime tomography has better options to acquire data in a longer setup (i.e. with a longer seismic line) as the signal to noise ration can be improved by stacking or a stronger source signal (Kearey et al., 2002). Therefore, the penetration depth of the traveltime tomography survey can be improved such that deeper parts of the diatreme could be imaged. Extending ERT lines on the other hand might be more challenging as with increasing electrode distance the measured signal becomes very weak. It is much harder to overcome that problem such that the limiting penetration depth is more shallow.

In addition to the ERT and the traveltime data, synthetic gravity measurements are generated. The resulting anomaly of the diatreme structure shows a magnitude of 0.3 mGal. Commercial gravimeters that are commonly used in gravimetric surveys measure the gravitational acceleration with an accuracy of approximately 0.01 mGal, some even provide an accuracy of 0.001 mGal (BGR, n.d.). Therefore, this anomaly should be clearly observable in gravimeter measurements in the field. Note that in the synthetic model, topographic effects were neglected and the 2D subsurface section was assumed to be horizontally layered around the diatreme. In reality, topography, subsurface heterogeneities, 3D effects or deeper structures like small volcanic intrusions might influence the measurements and limit the detectability. However, the gravity anomaly should be still be measurable. Depending on how accurate the gravity measurement are and how strong external factors are influencing the survey, gravity data could hold information about the deep subsurface below the depth of penetration of ERT or traveltime tomography. Since the ERT method and traveltime tomography image the upper 30 m quite accurate, a combination with a potential gravity data set could improve the deeper parts of a model or even extend it.

5 Conclusion

Aim of this project is to investigate how different geophysical methods are sensing a diatreme structure in a layered subsurface. The 2D synthetic data study showed, that electrical resistivity and traveltime tomography can image the diatreme, especially the upper boundary. Of all methods the Dipole-Dipole configuration returned the best image but as the method is prone to noise different more robust configurations and methods should be considered as well. Furthermore, section 4 discussed the lack of resolution close to the diatreme boundaries in the results of the traveltime tomography.

The upcoming Master thesis project will be based on previously acquired field data including the methods of seismic refraction, seismic reflection, magnetics and ERT. As data quality might cause difficulties during the joint inversion process or regions with data sparsity might be identified during the project, additional field data could be acquired to improve the modelling of the diatreme structure. The synthetic data study of this project suggests that ERT data is most suitable to recover information about the lateral boundaries of the diatreme as well as the shallow subsurface including the upper boundary of the diatreme. An ERT survey with the Dipole-Dipole electrode configuration should be complemented by other more robust configurations as the signal to noise ratio might cause troubles. For improving the imaging of deeper parts seismic refraction surveys with long receiver spreads and a stronger source like a shotgun needs to be considered. Also gravity data could be acquired to gain more information about deeper structures as the density contrast should result in an observable anomaly.

This work also stressed the importance of the regularization during the data inversion, namely the smoothing constraint. Here, the final inversion parameters were found using semi-random testing and the decision was purely based on the data misfit measure χ. Since the goal of the Master thesis research is the generation of an optimized data-driven model, further fine-tuning of the inversion parameters and more sophisticated criteria for the inversion constraint are necessary as it will lead to improvements of the inversion results and the resulting image of the volcanic diatreme structure.

References

BGR (n.d.). *Gravimetry*. URL: https://www.bgr.bund.de/EN/Themen/GG_Geophysik/Bodengeophysik/Gravimetrie/gravimetrie_node_en.html (visited on 01/14/2023).

Boxberg, Marc (2011). *Magnetische Kartierung zur Bestimmung der Lage des Phonolith Diatrems bei Rockeskyll, Westeifel: Bachelorarbeit*. Bochum.

Geldart, Lloyd P and Robert E Sheriff (2004). *Problems in exploration seismology and their solutions*. Society of Exploration Geophysicists.

Gilberti, Tim (2020). *Integration eines aus photogrammetrischen Messungen erstellten Modells der Oberflächentopographie in bestehende Integration eines aus photogrammetrischen Messungen erstellten Modells der Oberflächentopographie in bestehende geophysikalische Modelle eines vulkanischen Diatrems am Rockeskyller Kopf: Bachelorarbeit*. Bochum.

Günther, T, C Rücker, K Spitzer, et al. (2006). "3-d modeling and inversion of DC resistivity data incorporating topography-Part II: Inversion". In: *Geophys. J. Int* 166.2, pp. 506–517.

Hauburg, Nadine (2016). *3D-refraktionstomographische Untersuchung eines vulkanischen Diatrems am Rockeskyller Kopf: Masterarbeit*. Bochum.

Hopmann, PM (1914). "Spuren eines Phonolithdurchbruches bei Rockeskyll in der Eifel". In: *Zent. Mineral., Stutt.* 35, p. 565.

Johnson, Timothy C and D Wellman (2015). "Accurate modelling and inversion of electrical resistivity data in the presence of metallic infrastructure with known location and dimension". In: *Geophysical Journal International* 202.2, pp. 1096–1108.

Kearey, Philip, Michael Brooks, and Ian Hill (2002). *An introduction to geophysical exploration*. Vol. 4. John Wiley & Sons.

Lawson, Charles L and Richard J Hanson (1995). *Solving least squares problems*. SIAM.

Mertes, Hubertus (1983). *Aufbau und genese des Westeifeler Vulkanfeldes*. 9. Institut für Geologie der Ruhr-Universität-Bochum.

Mues, Hannah (2013). *Weiterführende magnetische Kartierung zur Ortung des Phonolith-Diatrems bei Rockeskyll, Westeifel: Bachelorarbeit*. Bochum.

Palacky, GJ (1988). "Resistivity characteristics of geologic targets". In: *Electromagnetic methods in applied geophysics* 1, pp. 52–129.

Plumpe, Niklas (2015). *Geoelektrische Tomographie eines Diatrems am Rockeskyller Kopf und Reinterpretation eines seismischen Profils: Bachelorarbeit*. Bochum.

Rücker, C, T Günther, and K Spitzer (2006). "3-d modeling and inversion of DC resistivity data incorporating topography–Part I: Modeling". In: *Geophys. J. Int* 166.2, pp. 495–505.

Rücker, C., T. Günther, and F. M. Wagner (2017). "pyGIMLi: An open-source library for modelling and inversion in geophysics". In: *Computers and Geosciences* 109, pp. 106–123. DOI: 10.1016/j.cageo.2017.07.011. URL: https://www.sciencedirect.com/science/article/pii/S0098300417300584.

Schmincke, Hans-Ulrich (2009). *Vulkane der Eifel: Aufbau, Entstehung und heutige Bedeutung*. Springer.

Schneider, Daniel (2017). *Oberflächennahe Reflexionsseismik über einem Diatrem am Rockeskyller Kopf: Bachelorarbeit*. Bochum.

Shewchuk, Jonathan Richard (1996). "Triangle: Engineering a 2D quality mesh generator and Delaunay triangulator". In: *Workshop on Applied Computational Geometry*. Springer, pp. 203–222.

White, James DL and P-S Ross (2011). "Maar-diatreme volcanoes: a review". In: *Journal of Volcanology and Geothermal Research* 201.1-4, pp. 1–29.

Won, IJ and Michael Bevis (1987). "Computing the gravitational and magnetic anomalies due to a polygon: Algorithms and Fortran subroutines". In: *Geophysics* 52.2, pp. 232–238.

Zelt, Colin A (2021). "Traveltime tomography using controlled-source seismic data". In: *Encyclopedia of solid earth geophysics*. Springer, pp. 1828–1848.

A Appendix

A.1 Settings for forward and inverse computations

Table A1: Settings for forward computations.

Method	**Parameter**	**Value**
ERT	first electrode	-30 m
	last electrode	120 m
	number of electrodes	76
	noise level	2.5 %
	absolute noise	0.001 mV
Traveltime Tomography	first sensor	-40 m
	last sensor	140 m
	number of sensors	91
	shot spacing	6 m
	noise level	0.01 %
	absolute noise	1 ms
Gravity	first sensor	-20 m
	last sensor	120 m
	number of sensors	71

Table A2: Settings for inversions.

Parameter	ERT - DD	ERT - SLM	ERT - WA	Traveltime Tomography
secNodes	2	2	2	2
paraMaxCellSize	20	20	20	20
lam	3	17	17	2.5
zWeight	0.3	0.2	0.3	-
vTop	-	-	-	600
vBottom	-	-	-	2700

A.2 Data management

Software Data processing, inversions and modelling will be performed in open-source packages in Python (e.g. PyGIMLI, Numpy etc.). It is possible that SeismicUnix or Reflexw will be used for seismic data inspection.

Inputs Input data for the Master thesis research will be previously acquired field data. A summary of the different data is shown in table A3. As the data was acquired as part of previous thesis works at the Ruhr-Universität Bochum and not published yet, thos files will be stored in a final repository which will be made available for the supervisors. This will possibly be done via Sciebo. This will be done as well with additional data that might be acquired as part of this thesis work.

Table A3: Overview of input data.

Method	Year	Size
Magnetics	2011	1.6 MB
	2012	212 KB
ERT	2015	158 MB
	2020	128 KB
Seismics	2015	683 MB
	2017	656 MB
Photogrammetry	2020	12 GB
		Total: 14 GB

Outputs outputs: Formats, data size, where stored Intermediate and final results of the thesis work include processed data, inversion results in form of models, Python scripts and Figures generated to visualize results. Those will be stored in a Github repository which will be made available for the supervisors. For the time of the research this repository will be kept private. However, after finishing the thesis work the repository might be made public depending on the outcome of the thesis work. Also, the report in form of .tex and other LaTeX-formats will be stored in the repository to ensure version control of the writing process. It also makes an easy access and commenting for the supervisors possible.